Oxygen Reduction Electrocatalysis Using N-Doped Graphene Quantum-Dots

1 AUTHOR:

Wissam A. Saidi
University of Pittsburgh
94 PUBLICATIONS **874** CITATIONS

Oxygen Reduction Electrocatalysis Using N-Doped Graphene Quantum-Dots

Wissam A. Saidi*

Department of Chemical and Petroleum Engineering, University of Pittsburgh, Pittsburgh, Pennsylvania, 15261, United States

 Supporting Information

ABSTRACT: First-principles investigations of the electrocatalytic activity toward the four-electron oxygen reduction-reaction in N-doped graphene quantum dots reveal that pyridinic and graphitic nitrogen are the most active sites with overpotentials of 0.55 and 0.79−0.90 V, respectively. This agrees with experimental findings. Our calculations account for van der Waals interactions, solvent effects, and describe the electrochemistry using standard hydrogen electrode model. The results show correlations between OH*, OOH*, and O* binding energies that impose a lower limit on the oxygen reduction overpotential.

SECTION: Energy Conversion and Storage; Energy and Charge Transport
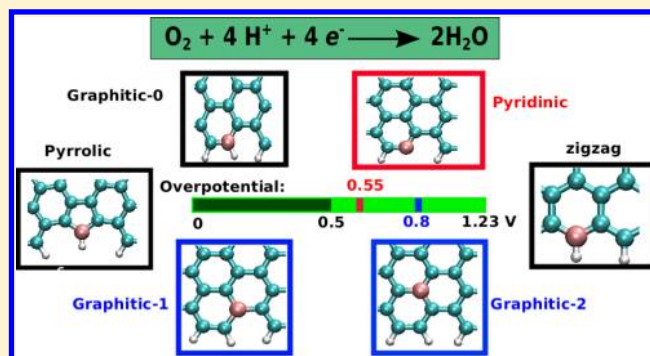
The oxygen reduction reaction (ORR) and its reverse reaction, oxygen evolution reaction (OER), are among the most studied electrochemical reactions for fundamental reasons as prototypes of four electron transfer reactions, and for technological relevance in renewable energy production. Specifically, both ORR and OER are at the center of many applications in electrochemical energy conversion processes including polymer electrolyte membrane fuel cells (PEMFCs), direct-solar and electrolytic water-splitting devices,[1] and metal−air batteries.[2] However, a key element for the commercialization of these reactions is the need of an efficient and cost-effective catalyst that solves their slow kinetics at the oxygen electrodes, namely, the cathode in fuel cells and the anode in electrolyzers. For example, Pt-based alloys are among the best catalysts in PEMFCs despite the fact that the fuel cells have a significant power loss due to a low operating voltage of 0.7 V as measured with respect to standard hydrogen electrode (SHE); this is only 57% of the available free energy.[3,4] Additionally, and more importantly, large amounts of the precious metal Pt are needed to boost the cathode kinetics that are significantly slower than the hydrogen evolution at the anode.

Currently, nanocarbon materials are heavily researched not only as a support to efficiently disperse catalytic particles,[5,6] but also as novel and cheap catalytic materials.[7,8] In particular, N-doped carbon materials have attracted a lot of interest as a potential metal-free catalysts for ORR.[9−22] Matter et al. showed ORR activity using N-doped carbon nanofiber, which was particularly high in the presence of Fe.[9,11] Gong et al. demonstrated high ORR activity in N-doped carbon nanotubes as well but without any metals.[17] Several groups have reported that N-doped graphene (N-GA) exhibited catalytic activity toward ORR in both alkaline[18,19] and acidic[14,23,24] media. Also,

recently, N-doped graphene quantum-dots (N-GQD) showed ORR activity with a greater potential than Pt-based PEMFCs, but nevertheless led to currents comparable to that of Pt.[25,26] In these N-GQDs, and in contrast to nitrogen-doped nano-carbons,[27] the ORR activity did not show a positive correlation with the nitrogen content.

The ORR mechanism in N-doped nanocarbons including the active site is still a matter of debate despite prior studies.[9−12] Experimentally, Matter et al. concluded that pyridinic nitrogen is the only active site, while Subramanian reports that both pyridinic and graphitic nitrogen can activate the ORR process.[9,14] On the basis of density functional theory (DFT) investigations, Okamoto proposed that the complete four-electron ORR activation can be achieved with an adequate binding energy of the oxygen atom on multiple N-doped graphitic sites.[15] Ikeda et al. also concluded similarly that graphitic nitrogen was the active site based on oxygen adsorption barriers and energetics of the subsequent ORR processes.[12] Recently, Kim et al. proposed that the ORR activation initiates at the outermost graphitic nitrogen site with the first reduction step; however, the latter graphitic nitrogen becomes pyridinic-like in the next reduction steps via the ring-opening of a cyclic C−N bond.[21]

In this Letter, we investigate the ORR activity in N-GQDs and the effect of the nitrogen doping-site chemistry on the efficiency of the electrochemical reaction. The ORR can be carried out incompletely using a two electron pathway that reduces O_2 to H_2O_2, or completely using a four-electron
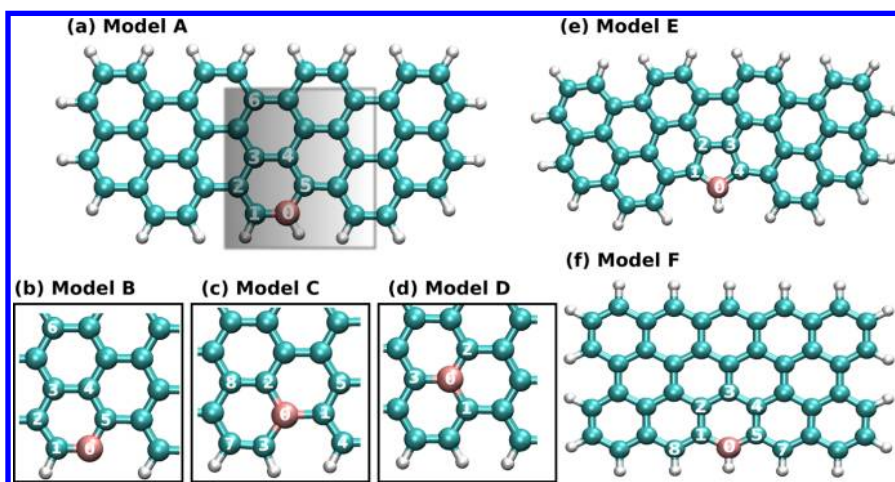
Figure 1. Six different models for the N-GQDs. Models **B**, **C**, and **D** are similar to **A** except in the atom arrangement inside the shaded box. Potential reaction sites are labeled. Hydrogen is white, carbon is turquoise, and nitrogen is pink.

process that reduces O_2 to 2 H_2O. Here we study the complete reduction cycle because the Koutechy–Levich plots recently showed that the ORR proceeds in N-GQDs through the four-electron mechanism.[26] The O_2 reduction is carried out using intermediate species associated with one electron transfer at a time,[28] which is energetically more favorable than the simultaneous transfer of more than one electron, as stipulated by Marcus theory.

There are two main reaction paths for the complete four-electron reduction of O_2 into H_2O: associative and dissociative. In both cases, electron and proton transfer takes place until full reduction where the associative path commences with the reduction of O_2 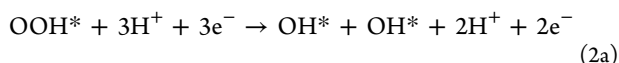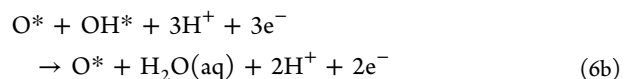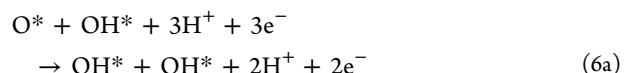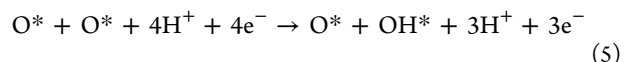directly to OOH (also known as peroxo path), while in the dissociative path, O_2 dissociates first on the surface to 2O* before it is reduced. In this study, we assume that the electron and proton transfer takes place simultaneously similar to what has been done in metallic and oxide materials.[28,29] The associative mechanism is summarized using the following four elementary steps:

$$O_2(g) + 4H^+ + 4e^- \rightarrow OOH^* + 3H^+ + 3e^- \tag{1}$$

$$OOH^* + 3H^+ + 3e^- \rightarrow OH^* + OH^* + 2H^+ + 2e^- \tag{2a}$$

$$OOH^* + 3H^+ + 3e^- \rightarrow O^* + H_2O(aq) + 2H^+ + 2e^- \tag{2b}$$

$$OH^* + OH^* + 2H^+ + 2e^- \rightarrow OH^* + H_2O(aq) + H^+ + e^- \tag{3a}$$

$$O^* + H_2O(aq) + 2H^+ + 2e^- \rightarrow OH^* + H_2O(aq) + H^+ + e^- \tag{3b}$$

$$OH^* + H_2O(aq) + H^+ + e^- \rightarrow * + 2H_2O(aq) \tag{4}$$
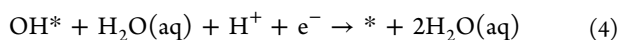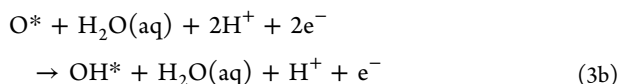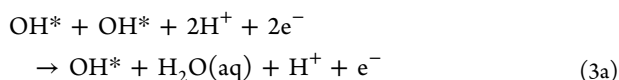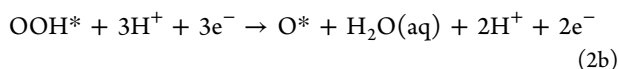
There are two branching paths for the second and third steps, where OOH is reduced to 2 OH* in path (a) defined in eq 2a, and to O* and H_2O in path (b) defined in eq 2b. Both paths lead to the same final products in the third step as shown in eqs 3a and 3b. The dissociative mechanism proceeds similarly to the associative mechanism except that the first two steps differ as shown below:

$$O^* + O^* + 4H^+ + 4e^- \rightarrow O^* + OH^* + 3H^+ + 3e^- \tag{5}$$

$$O^* + OH^* + 3H^+ + 3e^- \rightarrow OH^* + OH^* + 2H^+ + 2e^- \tag{6a}$$

$$O^* + OH^* + 3H^+ + 3e^- \rightarrow O^* + H_2O(aq) + 2H^+ + 2e^- \tag{6b}$$

The efficiency of the ORR process is determined by examining the reaction free-energies of the different elementary steps, where the one with the smallest reaction free-energy is the rate-limiting step (RLS). This thermodynamic approach establishes a minimum set of requirements for the facile reaction based on the binding of the intermediates because it assumes there are no extra barriers from, e.g., adsorption/dissociation of O_2 or proton/electron transfer reactions. The theoretical justification is based on the Brønsted–Evans–Polanyi postulate,[30] which stipulates that the changes in the activation energy of an elementary step follow the changes of the reaction energy. Additionally, this methodology was applied before successfully to different systems.[28–30]

To connect with experimental results, we use the RLS to determine the overpotential η of the fuel cell defined as the difference between the equilibrium potential of the ORR process per step ($U_0 = 4.92/4 = 1.23$ V) and the lowest potential where all steps are downhill. This definition assumes that the binding energies are independent of the applied voltage, which is generally a good approximation.[31]

We have considered a single nitrogen substitutional doping using ten different models for the graphene GQD, six of which are shown in Figure 1. The chemistry of the single nitrogen doping is expected to be prevalent because nitrogen aggregation is inhibited on pristine graphene due to the repulsive interaction between nitrogen dopants.[32] In Models **A**, **C**, and **D**, the nitrogen doping is a graphitic-like substitution where the nitrogen is located at different distances from the GQD edge. Model **B** has a pyridine-type doping that is similar to Model **A** except that one methine ═CH─ group is replaced by nitrogen. The pyridinic nitrogen is particularly interesting as it possesses one lone pair of electrons in addition to the one electron donated to the conjugated π bond. In **E**, nitrogen belongs to a five-membered ring with a pyrrole-like doping.

These models are motivated by experiment where the employed different nitrogen functional forms have been observed in carbonaceous materials.[27,33] Also, for completeness, we considered GQDs with zigzag-type edges that correspond to the arm-chair models **A**, **C**, and **D**. The zigzag-type model that corresponds to **A** is shown as Model **F** in Figure 1. Out of the ten GQD models investigated, we only selected six models that are the most stable in aqueous environments (see Supporting Information (SI) for more details).

The thermochemistry of the electrochemical reactions is studied using DFT calculations in conjunction with SHE model pioneered by Nörskov, Rossmeisl, and co-workers.[28,29,34,35] The quantum chemical calculations are carried out using the all electron FHI-aims program[36] employing PBE exchange-correlation functional[37] and DFT+vdW dispersion corrections[38] (more details are given in the SI). In the adopted SHE approach to electrochemistry, zero voltage is defined based on reversible hydrogen electrode, where protons and electrons are in equilibrium with hydrogen gas, i.e., chemical potential for proton−electron pair is equal to that of $H_2(g)$. The influence of the applied potential is included to "first order" by shifting the Gibbs free-energies by $\Delta G(U) = neU$ where e is the electron charge, n is the number of electrons transferred during the reaction step, and U is the electrode potential measured with respect to SHE. This approach was previously validated by comparing to more accurate modeling,[39] and also successfully described the electrochemical reactions on different systems.[28,29,34,35]

The reaction free-energies are computed from the Gibbs free-energy at standard conditions ($T = 298$ K, $p_{H_2} = 1$ bar, and pH = 0), and defined as

$$\Delta G = \Delta G_0 + \Delta G(U) + \Delta G_{aq} \qquad (7)$$

Here $\Delta G_0 = \Delta E + \Delta E_{ZPE} - T\Delta S$, where ΔE is the DFT reaction energy, ΔE_{ZPE} is the difference in the zero-point energies, $T\Delta S$ is the entropic contribution calculated from standard tables for the gas phase molecules (contributions from phonons are much smaller at room temperature and are thus neglected). ΔE is computed using H_2 and H_2O as a reference. More details are given in the SI.

The effect of the water environment on reaction free-energies captured by ΔG_{aq} in eq 7 originates from hydrogen bonding between the water molecules and the different GQD adsorbates. To a very good approximation, the binding energy of adsorbate **X** in the presence of the solvent can be written as $\Delta E_X(aq) = \Delta E_X + \Delta E_{ww} + \Delta G_{aq}$, where ΔE_X is the binding energy without water and ΔE_{ww} is the water−water interaction. This definition can be used to compute the effect of the solvent on the binding energies. In practice, $\Delta E_X(aq)$ is computed by performing simulations with 2−6 water molecules that are placed in the proximity of the doping site, and relaxing all degrees of freedom in the system. The obtained ΔG_{aq} was not very sensitive to the number of water molecules where the values varied to less than ±0.15 eV with the different number of solvent molecules. The stabilization energy ΔG_{aq} for the ORR intermediate species of eqs 1−6 are summarized in Table S2. The results are in very good agreement with recent values obtained using more computationally elaborate schemes,[40] as detailed in SI.

The reaction free-energies ΔG_0, ΔG_1, ΔG_2, and ΔG_3 for the four reduction steps can be readily computed using eq 7 from the optimum binding energies discussed in Tables S3 and S4

and Figures S1, S2, and S3. The ΔG values are shown in Figures S4 and S5 for the associative and dissociative paths. Here it is important to note that the total free energy of the ORR is fixed at $\Delta G = 4.92$ eV, and the optimal catalyst divides this energy equally between the four charge transfer processes. That is, ideally, the free energies of the individual steps should be fixed at 1.23 eV. If an elementary reaction becomes highly exothermic, then this will indicate that one or more of the other elementary steps is endothermic. In this case, the step with the smallest reaction free-energy is the RLS that retards the fuel cell performance.

We summarize the ORR overpotential η of the different models in Table 1. The pyridinic model **B** has the smallest

Table 1. A Lower Estimate for the Overpotential η in V for the Six N-GQD Models[a]

| | associative | | dissociative | |
model	a	b	a	b
A	–	–	–	–
B	–	–	1.15	0.55
C	0.86	0.86	0.86	0.86
D	0.79	0.79	0.79	0.92
E	–	–	1.18	0.81
F	1.18	1.18	0.71	0.82

[a]Routes (a) and (b) for the associative and dissociative mechanisms are shown separately.

value $\eta = 0.55$ V from the dissociative channel, while the associative one is not active. The graphitic-like models where the doping is far from the GQD edges as in **C** and **D** have a larger $\eta = 0.79-0.90$ V than the pyridinic model **B**, and thus leads to less efficient fuel cells. However, this doping chemistry is particularly interesting, as both the associative and dissociative paths are active with similar η values. The zigzag edge GQD is also active in the dissociative step with a $\eta = 0.7-0.8$ V, while the associative mechanism is blocked. The results show that the pyridinic and the graphitic sites are the most active for ORR, which agrees with previous experimental results.[9,14]

To explain the onset potential for each doping chemistry model, we determine the RLS by examining ΔG values for the elementary reaction steps. For the associative mechanism, the RLS for Models **B**, **E**, and **F** is associated with the first reduction step due to weak stabilization of OOH* as measured with respect to the ideal limit, as shown in Figure S4. On the other hand, for **A**, OOH* is stable but OH* is strongly bound with $\Delta G_3 < 0$ that blocks the ORR process in the second reduction step. Models **C** and **D** have optimum binding of OOH* but they overbind OH*, and thus OH* activation is the RLS. For the dissociative path, the RLS is the same as in the associative path for strong OH* bonding. This is the case for **A**, **C**, and **D**. For **B**, the RLS is due to the second reduction step measured by ΔG_1 (coadsorption of 2OH*) or third reduction step measured by ΔG_2 (adsorption of O*). ΔG_2 also determines the RLS for **F**. For **E**, the strong coadsorption of OH* and O* has the smallest reaction free energy that is similar to the associative path where the OOH* is also weakly bound.

Charge analysis show that GQD donates electrons to nitrogen, where most of this charge is donated from the nearest-neighbor carbon atoms of nitrogen that become positively charged.[12,15,40] This charge transfer can be under-
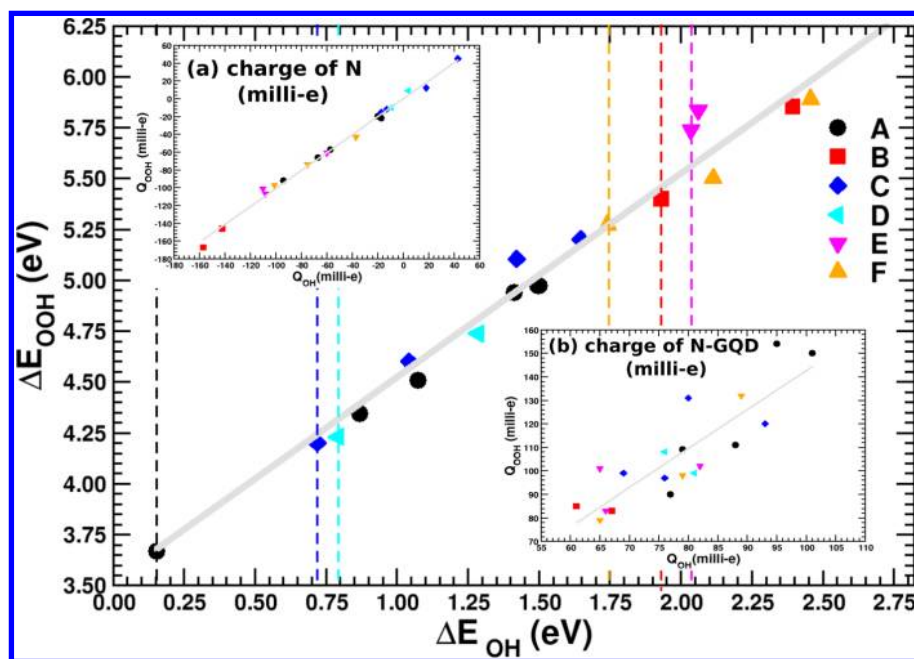
Figure 2. Direct correlation between the binding energies of OOH* and OH* for the same adsorption site on the six different models of the GQDs shown in Figure 1. The best fit line for the total energies and Gibbs free-energies is $\Delta E_{OOH} = \Delta E_{OH} + 3.53$ and $\Delta G_{OOH} = \Delta G_{OH} + 3.46$ eV. The optimum binding energy for each GQD is indicated by a dashed line. Inset (a) shows the correlation between total charge on nitrogen for the different adsorption configurations shown in the main figure. Inset (b) is similar to (a) except that it shows the correlation between the total charge transferred from GQD to OH* and OOH*.

stood because nitrogen has a larger electronegativity value than carbon. However, we find that the reactivity of the N-GQD toward OOH* and OH* activation correlates with the availability of spin density on the neighboring carbon atoms to the doping site.[41]

The adsorption of O_2 on the different GQDs was also investigated, as O_2 should adsorb on the GQD first to initiate the ORR. In the absence of a H_2O solvent, we find that for all the GQD models with the exception of **A**, O_2 is in a physisorption configuration judging by the relatively large separation 2−3 Å between O_2 and the GQD, and the absence of any rumplings on the GQD surface. This is consistent with previous investigations.[10,15,40] For **A**, O_2 chemisorbs in atop configuration at site 1 (see Figure S6). These results can be explained because the adsorption of O_2 on the carbon reactive sites that are close to nitrogen is not favorable due to repulsive interactions between the lone pair electrons of oxygen and nitrogen. As discussed before, the solvent has significant effect on the stability of the adsorbates, and it is found that water solvent can stabilize O_2 on the N-GA[40] where the stabilization energy is almost a factor of 2 larger than that of OH. This was validated for the pyridinic model **B** where O_2 can adopt different adsorption configurations, as shown in Figure S6. The solvent is also expected to bind O_2 to the other GQD models.

The analysis of the GQDs efficiency toward the ORR activation is compounded by the fact that the reaction free-energies are dependent on the GQD model and the doping chemistry. Thus, it is not clear whether the values of the overpotential are applicable to other GQDs. However, we find that this is not the case due to existing correlations between the binding energies of OOH* and OH*, and between OH* and O* for some GQD models. These correlations impose constraints on the overpotential as we will show below.

Figure 2 shows the binding energy of OH* vs OOH* for the same adsorption site, where for each GQD we include few of

the lowest energy configurations. Assuming a linear relationship between the binding energies with a slope of unity, the best fit line for total energies is $\Delta E_{OOH} = \Delta E_{OH} + 3.53$ eV in vacuum and $\Delta G_{OOH} = \Delta G_{OH} + 3.46$ eV in aqueous solution (not shown).[42] The slope of 1 in the linear fit is motivated by the single bond between O and the carbon of N-GQD for both OH* and OOH*.[43] The difference in adsorption energy between OH and OOH is in good agreement with previous studies on N-doped graphene GQDs.[20,40,41] As seen from the figure, the linear fit describes very well the results over a one-order-of-magnitude wide range of the OH* adsorption energy, which is a strong indication of the validity of the model. The constant energy difference between the binding energies of OH* and OOH* was also reported before as 3.2 and 3.29 eV on metal (111) and (100) facets, respectively,[34] 3.00 eV for oxide surfaces[43] and 3.10 eV for metal doped graphene.[44] The fact that this behavior applies over a wide range of materials including solids and clusters, and with different electronic structures, metals versus insulators, shows the universality of this scaling behavior.

The direct correlation between the binding of OH* and OOH* stems from their similar interactions with the GQD as exemplified by their similar adsorption sites. To gain better insight and show that this is indeed the case, we examined the partitioning of the electronic charge, namely, the total charge transfer from the GQD to nitrogen, OH* and OOH* in the different binding configurations. Inset (a) of Figure 2 shows that the total charge on nitrogen is nearly the same between the equivalent OH* and OOH* configurations,[45] and that charge is donated from the GQD to nitrogen for the lowest energy adsorption configurations. Additionally, OH* and OOH* accept charge from the N-GQDs, and there is also a direct correlation between these charges, as shown in Inset (b) of Figure 2.[45] More charge is transferred to OOH* than OH* where the charge on the oxygen of OOH* closest to the GQD

is nearly a factor of 2 smaller than that of oxygen of OH*, which corroborates the weaker bonding to the N-GQD of OOH* compared to OH*.

The binding energy of O* and OH* to the GQDs are also correlated, but we find that this applies only for Models **A–D**. Figure S7 shows the optimum binding energies for OH* and 2 OH* plotted against the binding energies of O* and OH* + O*, respectively. The best fit line for these energies is $\Delta E_O =$ 0.44 ΔE_{OH}+2.03 eV in vacuum and $\Delta G_O =$ 0.44 ΔG_{OH} + 1.50 eV in aqueous solutions. The slope of $\approx$0.5 for the linear fit is motivated by the double bond of O* to the GQD compared to the single bond of OH*. The underpinnings of these correlations is the similarity of the binding sites between O* and OH* (see Table S3). The optimum configuration for oxygen is atop site **1** for **A**, epoxy **12** for **B**, and atop **3** for **C** and **D**. These binding sites are equivalent to those of OH* except in **B** where oxygen is not stabilized atop **1**. **E** and **F** show different behaviors than **A–D** for different reasons. In **E**, the lowest energy binding configuration of O* is different than OH* where O* bonds through a ring-opening of a cyclic C–N bond while OH* bonds in atop configuration on site **1**. On the other hand, for **F**, the binding sites for OH* and O* are the same, but their binding energies probably belong to a different linear trend than arm-chair Models **A–D**.

The importance of the correlations between the binding energies of OH*, OOH*, and O* is that it sets a limit on the minimum thermodynamic overpotential for ORR on the N-GQDs. Using the scaling relations between OH*, OOH*, and O*, we construct a volcano plot in Figure S8 where the binding energy of O* serves as the general descriptor for the ORR efficiency. This applies only for GQD models **A–D**, although there might be a general descriptor other than the O* binding energy that can be used in a volcano plot to describe the ORR activity of all GQDs. As seen from Figure S8, the ORR activity is the highest if the oxygen binds to N-GQD with $\Delta E_O \approx 2.3$ eV. The pyridinic-type doping with $\Delta E_O = 2.9$ eV is the closest to this optimum value.

Using the OH* and OOH* scaling relations, we can obtain a stronger constraint on η for the associative or peroxo path where OH* and OOH* are two intermediate species. The constant energy difference between OH* and OOH*, ΔG_{OOH} − ΔG_{OH} = 3.46 eV, indicates that the remaining electrochemical potential (4.92 − 3.46) = 1.46 V is to be divided between the two remaining steps. If the catalyst is ideal, this will be divided equally, and the remaining steps would have an activation energy of U_{min} = 1.46/2 = 0.73 V. Therefore, the minimum value of the overpotential in this case is η_{min} = 1.23− 0.73 = 0.5 V for ORR in the peroxo path regardless of the GQD model, at least in the low nitrogen doping limit. This value is larger than the recently calculated η_{min} = 0.37 ± 0.1 V for metal Pt electrodes,[34] which agrees with the experimental results that N-GQDs show less ORR activity than Pt-based PEMFC.[25,26] Among the different models investigated in this study, the graphitic doping has the smallest overpotential in the associative mechanism, but still this is $\approx$80% larger than 0.5 V. The lower limit η_{min} = 0.5 V obtained in the associative path is perhaps a more stringent constraint for the ORR process because the dissociation barrier for O_2 is larger than the hydrogenation barrier in N-doped graphene, which makes the associative path more favorable.[15,40]

In summary, we investigated the effect of the nitrogen doping-site chemistry on the ORR activity in N-GQDs based fuel cells. The efficiency of the O_2 reduction is analyzed using the free energies of intermediate species, and thus this imposes a lower limit on the overpotential of the ORR mechanism. Motivated by experimental observations of the doping site chemistry, different models of the GQD were employed including pyridinic–, pyrrolic– and graphitic–like nitrogen-doping. We show that the pyridinic-type doping has the smallest overpotential η = 0.55 V in the dissociative mechanism while the peroxo mechanism is blocked by weak OOH* adsorption. The graphitic-type doping far from the GQD edges shows ORR activity in both dissociative and associative paths with an overpotential value of η = 0.79−0.90 V. These findings are in very good agreement with experimental results which concluded that the pyridinic- and graphitic-type doping are the dominant active sites for ORR in N-doped nanocarbons. Additionally, we show that there is a universal relationship between the binding energies of OH* and OOH*, and between OH* and O* for selected GQD models. Using these scaling relations, the ORR efficiency can be described using an activity volcano plot with a single descriptor based on oxygen binding energy. Additionally, the OH* and OOH* correlations in the binding energies impose a lower limit of 0.5 V on the overpotential of the oxygen reduction using N-GQDs, at least if the doping chemistry is dictated by the single nitrogen atom type. The existing scaling relations between OH*, OOH*, and O* are similar to what has been seen before on metal and oxide surfaces, and show that the limitations of the ORR efficiency at the oxygen electrode are more universal than originally anticipated.

■ ASSOCIATED CONTENT

Ⓢ Supporting Information
Computational approach, stability of the GQD models, and adsorption geometries. This material is available free of charge via the Internet at http://pubs.acs.org.

■ AUTHOR INFORMATION

Corresponding Author
*E-mail: alsaidi@pitt.edu.

Notes
The authors declare no competing financial interest.

■ ACKNOWLEDGMENTS

■ REFERENCES

(1) Gray, H. B. Powering the Planet with Solar Fuel. *Nat. Chem.* **2009**, *1*, 7−7.

(2) Armand, M.; Tarascon, J.-M. Building Better Batteries. *Nature* **2008**, *451*, 652−657.

(3) Gasteiger, H.; Kocha, S.; Sompalli, B.; Wagner, F. Activity Benchmarks and Requirements for Pt, Pt-Alloy, and Non-Pt Oxygen Reduction Catalysts for PEMFCs. *Appl. Catal. B: Environ.* **2005**, *56*, 9−35.

(4) Gasteiger, H. A.; Markovic, N. M. Just a Dream- or Future Reality? *Science* **2009**, *324*, 48−49.

(5) Guo, S.; Sun, S. FePt Nanoparticles Assembled on Graphene as Enhanced Catalyst for Oxygen Reduction Reaction. *J. Am. Chem. Soc.* **2012**, *134*, 2492−2495.

(6) Wu, Z.-S.; Yang, S.; Sun, Y.; Parvez, K.; Feng, X.; Müllen, K. 3D Nitrogen-Doped Graphene Aerogel-Supported Fe_3O_4 Nanoparticles as

4164

dx.doi.org/10.1021/jz402090d | *J. Phys. Chem. Lett.* 2013, 4, 4160−4165

Efficient Electrocatalysts for the Oxygen Reduction Reaction. *J. Am. Chem. Soc.* **2012**, *134*, 9082−9085.

(7) Su, D. S.; Perathoner, S.; Centi, G. Nanocarbons for the Development of Advanced Catalysts. *Chem. Rev.* **2013**, *113*, 5782−5816.

(8) Zhu, C.; Dong, S. Recent Progress in Graphene-Based Nanomaterials as Advanced Electrocatalysts Towards Oxygen Reduction Reaction. *Nanoscale* **2013**, *5*, 1753−1767.

(9) Matter, P. H.; Zhang, L.; Ozkan, U. S. The Role of Nanostructure in Nitrogen-Containing Carbon Catalysts for the Oxygen Reduction Reaction. *J. Catal.* **2006**, *239*, 83−96.

(10) Sidik, R. A.; Anderson, A. B.; Subramanian, N. P.; Kumaraguru, S. P.; Popov, B. N. O_2 Reduction on Graphite and Nitrogen-Doped Graphite: Experiment and Theory. *J. Phys. Chem. B* **2006**, *110*, 1787−1793 PMID: 16471746.

(11) Matter, P. H.; Wang, E.; Arias, M.; Biddinger, E. J.; Ozkan, U. S. Oxygen Reduction Reaction Activity and Surface Properties of Nanostructured Nitrogen-Containing Carbon. *J. Mol. Catal A: Chem.* **2007**, *264*, 73−81.

(12) Ikeda, T.; Boero, M.; Huang, S.-F.; Terakura, K.; Oshima, M.; Ozaki, J.-i. Carbon Alloy Catalysts: Active Sites for Oxygen Reduction Reaction. *J. Phys. Chem. C* **2008**, *112*, 14706−14709.

(13) Kurak, K. A.; Anderson, A. B. Nitrogen-Treated Graphite and Oxygen Electroreduction on Pyridinic Edge Sites. *J. Phys. Chem. C* **2009**, *113*, 6730−6734.

(14) Subramanian, N. P.; Li, X.; Nallathambi, V.; Kumaraguru, S. P.; Colon-Mercado, H.; Wu, G.; Lee, J.-W.; Popov, B. N. Nitrogen-Modified Carbon-Based Catalysts for Oxygen Reduction Reaction in Polymer Electrolyte Membrane Fuel Cells. *J. Power Sources* **2009**, *188*, 38−44.

(15) Okamoto, Y. First-Principles Molecular Dynamics Simulation of {O_2} Reduction on Nitrogen-Doped Carbon. *Appl. Surf. Sci.* **2009**, *256*, 335−341.

(16) Lefevre, M.; Proietti, E.; Jaouen, F.; Dodelet, J.-P. Iron-Based Catalysts with Improved Oxygen Reduction Activity in Polymer Electrolyte Fuel Cells. *Science* **2009**, *324*, 71−74.

(17) Gong, K.; Du, F.; Xia, Z.; Durstock, M.; Dai, L. Nitrogen-Doped Carbon Nanotube Arrays with High Electrocatalytic Activity for Oxygen Reduction. *Science* **2009**, *323*, 760−764.

(18) Qu, L.; Liu, Y.; Baek, J.-B.; Dai, L. Nitrogen-Doped Graphene as Efficient Metal-Free Electrocatalyst for Oxygen Reduction in Fuel Cells. *ACS Nano* **2010**, *4*, 1321−1326.

(19) Sheng, Z.-H.; Shao, L.; Chen, J.-J.; Bao, W.-J.; Wang, F.-B.; Xia, X.-H. Catalyst-Free Synthesis of Nitrogen-Doped Graphene via Thermal Annealing Graphite Oxide with Melamine and Its Excellent Electrocatalysis. *ACS Nano* **2011**, *5*, 4350−4358.

(20) Zheng, Y.; Jiao, Y.; Chen, J.; Liu, J.; Liang, J.; Du, A.; Zhang, W.; Zhu, Z.; Smith, S. C.; Jaroniec, M.; Lu, G. Q. M.; Qiao, S. Z. Nanoporous Graphitic-C_3N_4@Carbon Metal-Free Electrocatalysts for Highly Efficient Oxygen Reduction. *J. Am. Chem. Soc.* **2011**, *133*, 20116−20119.

(21) Kim, H.; Lee, K.; Woo, S. I.; Jung, Y. On the Mechanism of Enhanced Oxygen Reduction Reaction in Nitrogen-Doped Graphene Nanoribbons. *Phys. Chem. Chem. Phys.* **2011**, *13*, 17505−17510.

(22) Studt, F. The Oxygen Reduction Reaction on Nitrogen-Doped Graphene. *Catal. Lett.* **2013**, *143*, 58−60.

(23) Lee, K. R.; Lee, K. U.; Lee, J. W.; Ahn, B. T.; Woo, S. I. Electrochemical Oxygen Reduction on Nitrogen Doped Graphene Sheets in Acid Media. *Electrochem. Commun.* **2010**, *12*, 1052−1055.

(24) Tsai, C.-W.; Tu, M.-H.; Chen, C.-J.; Hung, T.-F.; Liu, R.-S.; Liu, W.-R.; Lo, M.-Y.; Peng, Y.-M.; Zhang, L.; Zhang, J.; Shy, D.-S.; Xing, X.-K. Nitrogen-Doped Graphene Nanosheet-Supported Non-precious Iron Nitride Nanoparticles as an Efficient Electrocatalyst for Oxygen Reduction. *RSC Adv.* **2011**, *1*, 1349−1357.

(25) Li, Y.; Zhao, Y.; Cheng, H.; Hu, Y.; Shi, G.; Dai, L.; Qu, L. Nitrogen-Doped Graphene Quantum Dots with Oxygen-Rich Functional Groups. *J. Am. Chem. Soc.* **2012**, *134*, 15−18.

(26) Li, Q.; Zhang, S.; Dai, L.; Li, L.-s. Nitrogen-Doped Colloidal Graphene Quantum Dots and Their Size-Dependent Electrocatalytic

(26) Li, Q.; Zhang, S.; Dai, L.; Li, L.-s. Nitrogen-Doped Colloidal Graphene Quantum Dots and Their Size-Dependent Electrocatalytic Activity for the Oxygen Reduction Reaction. *J. Am. Chem. Soc.* **2012**, *134*, 18932−18935.

(27) McClure, J. P.; Thornton, J. D.; Jiang, R.; Chu, D.; Cuomo, J. J.; Fedkiw, P. S. Oxygen Reduction on Metal-Free Nitrogen-Doped Carbon Nanowall Electrodes. *J. Electrochem. Soc.* **2012**, *159*, F733−F742.

(28) Nörskov, J. K.; Rossmeisl, J.; Logadottir, A.; Lindqvist, L.; Kitchin, J. R.; Bligaard, T.; Jonsson, H. Origin of the Overpotential for Oxygen Reduction at a Fuel-Cell Cathode. *J. Phys. Chem. B* **2004**, *108*, 17886−17892.

(29) Rossmeisl, J.; Dimitrievski, K.; Siegbahn, P.; Nörskov, J. K. Comparing Electrochemical and Biological Water Splitting. *J. Phys. Chem. C* **2007**, *111*, 18821−18823.

(30) Nörskov, J. K.; Bligaard, T.; Hvolbaek, B.; Abild-Pedersen, F.; Chorkendorff, I.; Christensen, C. H. The Nature of the Active Site in Heterogeneous Metal Catalysis. *Chem. Soc. Rev.* **2008**, *37*, 2163−2171.

(31) Karlberg, G. S.; Rossmeisl, J.; Nörskov, J. K. Estimations of Electric Field Effects on the Oxygen Reduction Reaction Based on the Density Functional Theory. *Phys. Chem. Chem. Phys.* **2007**, *9*, 5158−5161.

(32) Hou, Z.; Wang, X.; Ikeda, T.; Terakura, K.; Oshima, M.; Kakimoto, M.-a.; Miyata, S. Interplay between Nitrogen Dopants and Native Point Defects in Graphene. *Phys. Rev. B* **2012**, *85*, 165439.

(33) Wei, D.; Liu, Y.; Wang, Y.; Zhang, H.; Huang, L.; Yu, G. Synthesis of N-Doped Graphene by Chemical Vapor Deposition and Its Electrical Properties. *Nano Lett.* **2009**, *9*, 1752−1758.

(34) Viswanathan, V.; Hansen, H. A.; Rossmeisl, J.; Nörskov, J. K. Universality in Oxygen Reduction Electrocatalysis on Metal Surfaces. *ACS Catal.* **2012**, *2*, 1654−1660.

(35) Viswanathan, V.; Hansen, H. A.; Rossmeisl, J.; Nörskov, J. K. Unifying the 2e- and 4e- Reduction of Oxygen on Metal Surfaces. *J. Phys. Chem. Lett.* **2012**, *3*, 2948−2951.

(36) Blum, V.; Gehrke, R.; Hanke, F.; Havu, P.; Havu, V.; Ren, X.; Reuter, K.; Scheffler, M. Ab Initio Molecular Simulations with Numeric Atom-Centered Orbitals. *Comput. Phys. Commun.* **2009**, *180*, 2175−2196.

(37) Perdew, J. P.; Burke, K.; Ernzerhof, M. Generalized Gradient Approximation Made Simple. *Phys. Rev. Lett.* **1996**, *77*, 3865−3868.

(38) Tkatchenko, A.; Scheffler, M. Accurate Molecular Van Der Waals Interactions from Ground-State Electron Density and Free-Atom Reference Data. *Phys. Rev. Lett.* **2009**, *102*, 073005.

(39) Yeh, K.-Y.; Janik, M. J. Density Functional Theory-Based Electrochemical Models for the Oxygen Reduction Reaction: Comparison of Modeling Approaches for Electric Field and Solvent Effects. *J. Comput. Chem.* **2011**, 3399−3408.

(40) Yu, L.; Pan, X.; Cao, X.; Hu, P.; Bao, X. Oxygen Reduction Reaction Mechanism on Nitrogen-Doped Graphene: A Density Functional Theory Study. *J. Catal.* **2011**, *282*, 183−190.

(41) Zhang, L.; Xia, Z. Mechanisms of Oxygen Reduction Reaction on Nitrogen-Doped Graphene for Fuel Cells. *J. Phys. Chem. C* **2011**, *115*, 11170−11176.

(42) Using a linear fit for ΔE instead, we obtain $\Delta E_{OOH} = 1.04\Delta E + 3.47$ with a mean-square error of 0.10 eV.

(43) Koper, M. T. Thermodynamic Theory of Multi-Electron Transfer Reactions: Implications for Electrocatalysis. *J. Electroanal. Chem.* **2011**, *660*, 254−260.

(44) Calle-Vallejo, F.; Martinez, J. I.; Rossmeisl, J. Density Functional Studies of Functionalized Graphitic Materials with Late Transition Metals for Oxygen Reduction Reactions. *Phys. Chem. Chem. Phys.* **2011**, *13*, 15639−15643.

(45) For nitrogen charge, the best fit line has a slope of 1 and intercept of −0.4 milli-e. For GQD charge, linear fit has a slope 1.67 with intercept −24 milli-e.